Design of a compact, cryogen-free superconducting solenoid for the electron lens of the Fermilab Integrable Optics Test Accelerator (IOTA)

R.C. Dhuley,[a,*] **C. Boffo,**[a] **V. Kashikhin,**[a] **A. Kolehmainen,**[b] **D. Perini**[b] **and G. Stancari**[a]

[a]*Fermi National Accelerator Laboratory,*
P.O. Box 500, Batavia, Illinois 60510, U.S.A.

[b]*CERN,*
Esplanade des Particules 1, 1211 Meyrin, Switzerland

E-mail: rdhuley@fnal.gov

ABSTRACT: The proposed electron lens for Fermilab's Integrable Optics Test Accelerator (IOTA) will broaden its capabilities by enabling new research in nonlinear integrable optics, space-charge compensation, proton beam cooling, and more. The electron lens is based on a 5–10 keV, 1–2 A electron beam, shaped using a 0.7 m long, 0.8 T solenoidal magnetic field. A cryogen-free superconducting solenoid has been designed to provide this solenoidal field, taking into consideration the constraints on space, utilities, and infrastructure in the IOTA experimental hall. The solenoid is made of copper stabilized niobium-titanium conductor, conduction-cooled using 4 K closed-cycle cryocoolers. This paper describes the overall design of the solenoid encompassing its mechanical construction, current leads optimization, cryogenic thermal modeling that provides estimates of cooldown time and static/dynamic heat loads, and quench analysis.

---

*Corresponding author.

Contents

1 Introduction

The Integrable Optics Test Accelerator (IOTA) is a 40 m circumference storage ring at Fermilab, dedicated to beam physics, accelerator technology, and education [1]. A new electron lens is being built for IOTA. This lens will serve as a unique test bed for studying novel applications such as nonlinear integrable optics, space-charge compensation, generation of Landau damping, cooling of proton beams to reduce their emittance, and more. The electron lens will be made of a low-energy electron beam (5–10 keV, 1–2 A) generated by a thermionic gun and transported by solenoids and a toroidal section into the interaction region. The interaction region of the electron lens has a 0.8 T Main Solenoid with a warm bore enclosing a meter-long section of the main IOTA proton beam line. Figure 1 schematically shows the layout of the electron lens comprising of the Main Solenoid, an electron source and a collector, gun and collector solenoids, transport solenoids, and toroidal sections. Further details of the IOTA electron lens including development status and research plans are elaborated in refs. [1–3].

Electron lenses previously built for the Tevatron collider at Fermilab [4] and RHIC at Brookhaven National Laboratory [5], as well as the ones planned for LHC at CERN [6], require 5–7 T solenoidal fields. They use solenoids made of superconducting NbTi conductor cooled with liquid helium at ~ 4.5 K. For the 0.6 T electron-lens solenoid in SIS18 at GSI, on the other hand, a resistive magnet is being considered [7].
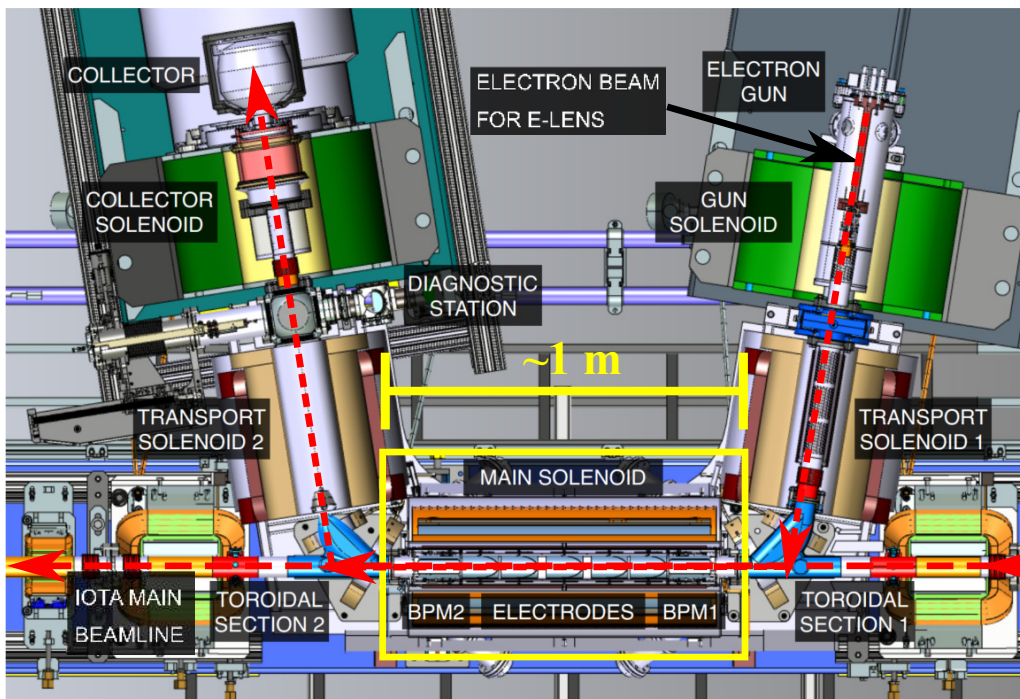
Figure 1. Layout of the components of the IOTA electron lens.

The IOTA electron lens Main Solenoid requires a field of 0.8 T. A superconducting option implies that the solenoid will be physically smaller than those for the Tevatron, RHIC and LHC, with less stored energy, looser quench protection requirements, and less stringent cryogenic cooling demands. A design study has been carried out using copper stabilized NbTi conductor, where the coil is conduction-cooled using 4 K cryocoolers. This paper presents electromagnetic, mechanical, and cryogenic aspects of the design study. To our knowledge, this is the first instance where an electron lens employs a cryogen-free superconducting magnet.

2 Main Solenoid design

2.1 Requirements and constraints

The electron lens requires a solenoidal field B_z of 0.8 T in a 'good field' region of at least 600 mm in length and 30 mm in diameter. Field homogeneity, B_r/B_z (B_r is the radial field), in the good field region should be $< 2 \times 10^{-4}$. The Main Solenoid assembly should possess a bore of diameter of at least 50 mm to accommodate the IOTA beam pipe, plus clearance for flanges, beam position monitors, feedthroughs, and other instrumentation.

Although the field and bore size requirements are modest, the existing IOTA beam line infrastructure puts space and weight constraints on the new electron lens. The Main Solenoid should preferably fit in a total longitudinal space of 1.4 m, so that the existing devices upstream and downstream (IOTA quadrupoles and related instrumentation) are not displaced (see figure 1). The lifting device in the IOTA experimental hall limits individual component weight to approximately 10 kN when lifting for assembly. We further note that although the IOTA hall does not have specific

constraints on utilities such as cooling water and electrical power, efforts must be made to keep additional installations to a minimum.

The constraint on the possible use of a superconducting solenoid is that the IOTA experimental hall, although adjacent to the FAST superconducting linac, does not have readily available cryogen supply and recovery facilities. A self-contained, dry cryocooling system must therefore be used. The solenoid should cool down to its base operating temperature within 24 hours so that the electron-lens downtime between successive experimental runs is reasonable. The cryocooling scheme should also be able to cool the solenoid to its base temperature within a few hours after recovering from a quench, in order to have a manageable impact on operations.

2.2   Evaluation of design options

Based primarily on the requirements of field and good field region, we evaluated resistive and superconducting options for the Main Solenoid. The resistive design uses a $20\,\mathrm{mm} \times 20\,\mathrm{mm}$ copper conductor with 15 mm diameter hole for cooling water. A copper stabilized NbTi conductor of size $1.25\,\mathrm{mm} \times 0.8\,\mathrm{mm}$ is selected for the superconducting option. This cable was used on a similar magnet designed at CERN for the AEGIS experiment [8]. Table 1 lists the design input parameters, namely coil turns, coil inner and outer diameters, and the operating current required to generate 0.8 T. The design output parameters, viz. the stored energy, coil weight, electrical and cooling requirements are also compared in table 1.

Table 1. Comparison of resistive and superconducting solenoid design options.

Parameter	Resistive solenoid	Superconducting solenoid
Conductor, size	Copper, $20\,\mathrm{mm} \times 20\,\mathrm{mm}$ (with dia. 15 mm hole for cooling water)	Copper stabilized NbTi, $1.25\,\mathrm{mm} \times 0.8\,\mathrm{mm}$
No. of layers	12	4
Turns per layer	34	480
Current at 0.8 T	1060 A	200 A
Solenoid ID/OD	125 mm / 618 mm	200 mm / 206.4 mm
Stored energy at 0.8 T	18.2 kJ	5.6 kJ
Mass of conductor	850 kg	19 kg
Cooling scheme	Forced water flow through the hole in the conductor	Conduction cooling with 4 K cryocoolers
Power consumption (magnet + cooling)	41 kWe	28 kWe

The superconducting solenoid outperforms the resistive solenoid in all of the criteria compared in table 1, mainly because superconductors can carry significantly higher current density ($> 500\,\mathrm{A/mm^2}$ for the chosen NbTi conductor) than resistive copper (typically limited to about $10\,\mathrm{A/mm^2}$, Wilson : 1983). Higher current density implies a smaller, lighter coil as well as a smaller operating current. For the present case, the superconducting coil has (a) five-fold smaller operating current, (b) three-fold smaller outer diameter (size of the coil), (c) three-fold smaller stored energy at 0.8 T, and (d) almost forty-fold smaller weight. The moderate size, weight, and stored energy in

the superconducting option makes it possible to use conduction cooling based on compact, closed-cycle 4 K cryocoolers. The total electrical power requirement for the superconducting solenoid is 28 kW assuming two Cryomech PT415 cryocoolers, which is smaller than the 41 kW needed for the resistive option. Cryocooler technology is mature, with demonstrated reliability in medical, industrial and research applications. The higher cost of a superconducting solution is also manageable. Low-frequency vibrations generated by the cryocoolers can be mitigated with mechanical dampers. Because of these considerations, the conduction-cooled superconducting option is clearly favored for the IOTA electron lens.

2.3 Mechanical design

The Main Solenoid uses commercial NbTi conductor manufactured by Luvata with its parameters listed in table 2.

Table 2. Parameters of the Luvata NbTi conductor.

| Parameter	Value
Dimensions	$1.25\,\text{mm} \times 0.8\,\text{mm}$
Nominal operating temperature	4.5 K
Critical current	550 A @ 4.5 T
Cu:NbTi ratio	4:1
Insulation	Kapton

The solenoid has one main coil that generates the 0.8 T solenoidal field. Four corrector dipole coils (two short coils upstream and two longer ones downstream) are used to adjust position and angle of the electrons in the lens and to control the overlap with the circulating beam. Additional trim layers are added at the two ends of the main coil to sustain the 0.8 T axial field at the edges. The main coil and the two trim coils are electrically connected in series. Table 3 shows parameters of the main coil and trim coils as well as the solenoidal fields produced by them when operated with a current of 200 A.

Table 3. Coil design parameters.

Parameter	Main coil	Trim coil (×2)
Length	600 mm	50 mm
Inner diameter	100 mm	100 mm
Turns = (No. of layers) × (turns per layer)	$1920 = 4 \times 480$	$280 = 7 \times 40$
Outer diameter	206.4 mm	211.2 mm
Central field at 200 A	0.8 T	1.4 T

Figure 2 shows a computer model of the Main Solenoid assembly. The main coil and the trim coils are first wound on the outer surface of an aluminum former, which also acts as a quench protection layer for the coils. After winding, the main and trim coils are impregnated in epoxy to prevent winding layer movement. A second cylindrical aluminum shell, called the main coil support, is added around the epoxy impregnated coils. The main coil support provides for attachment of the coil

hangers. Outside of the main coil support are the corrector coil and its support made of OFHC copper. The corrector coil support has slots to reduce its weight. Aluminum strain-relief posts for each of the ten current leads of the five coils are mounted on the main coil support, as depicted in figure 2.
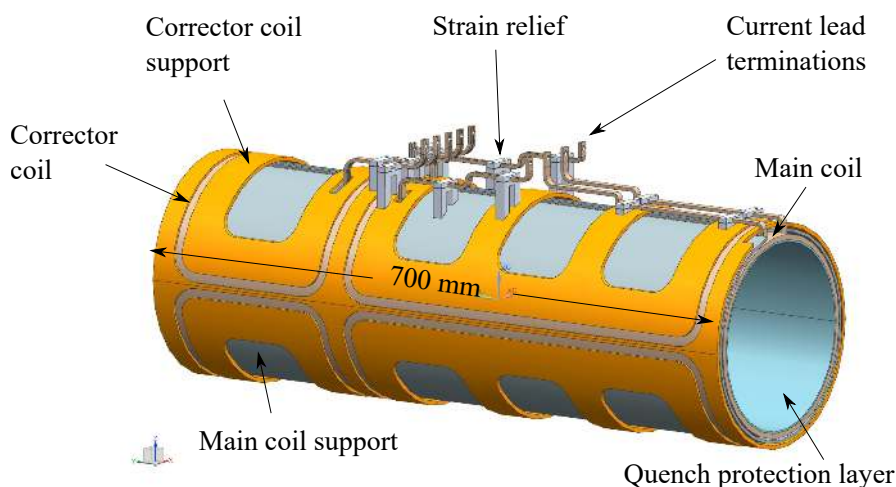

Figure 2. Model of the Main Solenoid assembly.

2.4 Magnetic field profile

Figure 3 shows the magnetic field profile computed in OPERA 3D. In the plots, $y = 0$ is the midpoint of the coil. The axial field plotted in figure 3a along the length of the solenoid shows approximately uniform 0.8 T field over a 0.5 m long region centered around the midpoint of the coil. The axial field falls steeply beyond this location, reaching 0.5 T at 0.35 m from the midpoint. This field profile falls short of the required 0.8 T over at least 0.6 m length showing that additional optimization of the coil is required. The relative radial component of the field is plotted in figure 3b along the solenoid length at $r = 15$ mm from the axis. The field homogeneity is 2.2% at $r = 15$ mm, $y = 0.3$ m. This does not satisfy the good field region requirement defined in section 2.1. Several options are being actively considered for lengthening the good field region beyond 0.6 m and reducing the field homogeneity below 0.02%. These include increasing the solenoid length, reducing the inner diameter, and inserting ferromagnetic plugs with 30 mm diameter holes at the coil edges.

3 Cryostat design

Due to the absence of liquid cryogen supply and recovery facilities in the IOTA experimental hall, a dry 4 K cryo-cooling scheme is proposed for the Main Solenoid. The dry, cryogen-free cooling system eliminates the piping required to circulate liquid/gaseous cryogens as well as a cryo-liquid bath that would otherwise be needed to cool the solenoid. Furthermore, the absence of cryogenic liquids and/or compressed gases eliminates the possibility of over-pressurization of the cryostat due to accidental scenarios such as a sudden loss of insulating vacuum or magnet quench. The cryogen-free cooling scheme thereby offers a compact cryostat with relaxed safety, operational procedures, and utility requirements.
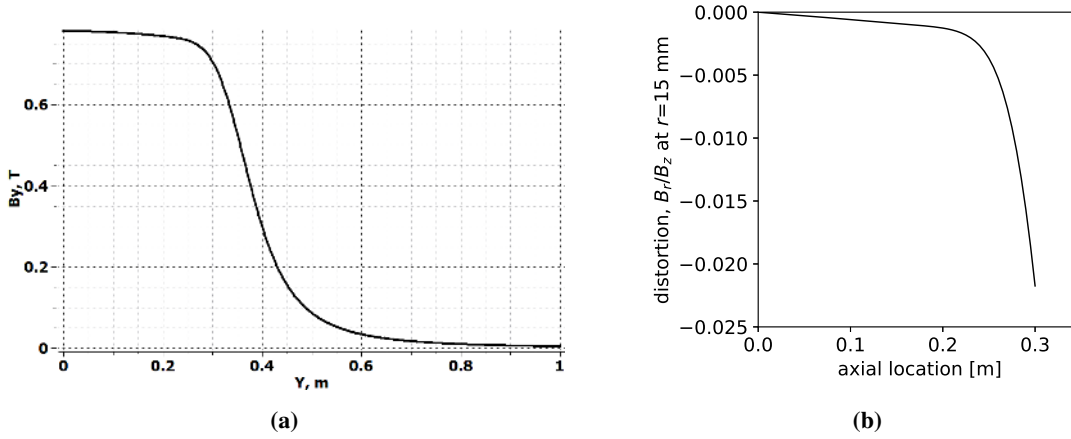
Figure 3. (a) Computed solenoidal field along the axis and (b) the ratio of radial to axial field at a radius $r = 15\,\mathrm{mm}$.

3.1 Main features of the cryostat

The Main Solenoid cryostat, depicted in figure 4, has the standard three-temperature level cooling scheme enabled by two-stage 4 K cryocoolers:

1. A vacuum vessel made of stainless steel SS304 operating at room temperature and enclosing all of the cold mass. The vessel is pumped to a vacuum $< 10^{-6}$ torr so that convective heat load to the cold mass inside is restricted to the level of residual gas conduction [10].
2. A thermal radiation shield made of aluminum alloy Al6061-T6 enclosing the Main Solenoid assembly and conduction cooled to the cryocooler stage 1 inside the vacuum vessel. The thermal shield is wrapped with multi-layer insulation to reduce the radiation heat load on cryocooler stage 1.
3. The Main Solenoid assembly conductively connected to the cryocooler stage 2 and enclosed by the thermal radiation shield.
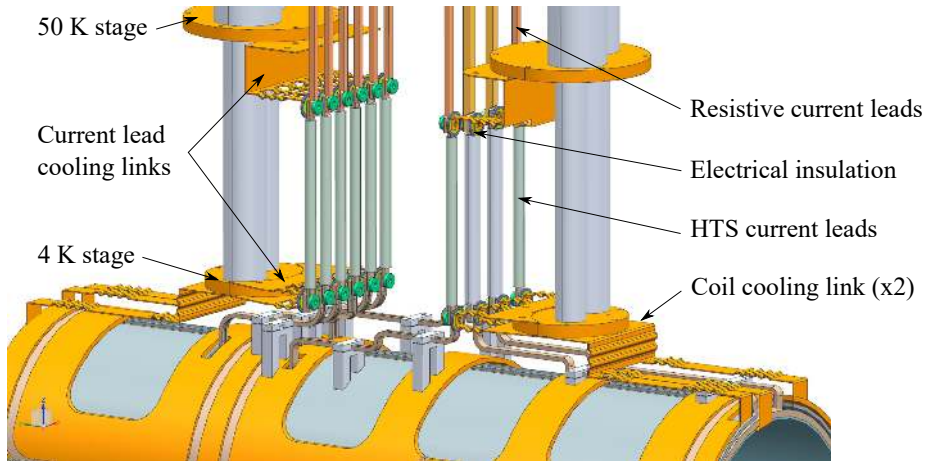
3.2 Current leads

The five pairs of current leads are arranged inside the cryostat, as depicted in figure 5. The composite leads include phosphor bronze sections (resistive leads) between room temperature and cryocooler stage 1 followed by HTS-110 Cryosaver$^{\mathrm{TM}}$ sections (BSSCO HTS leads [11]) between cryocooler stage 1 and stage 2. The colder ends of the HTS leads are connected to the coil NbTi terminations coming from the coils.

During solenoid operation, the heat flow to cryocooler stage 1 through the resistive leads comprises of ambient heat conduction and Joule dissipation in the leads. The resistive leads are designed with optimal length to cross section area ratio, L/A_{CS}, to minimize the total heat load to cryocooler stage 1. The optimization was done by numerically solving McFee's equation [12]:

$$\frac{L}{A_{\mathrm{CS}}} = \frac{1}{I^2}\left[\sigma(T_L)Q_{L,\mathrm{min}} + I\int_{T_L}^{T_H}\left(\frac{d\sigma(T)}{dT}\left(2\int_T^{T_H}\frac{k(T)}{\sigma(T)}\,dT\right)^{1/2}\right)dT\right],\qquad(3.1)$$
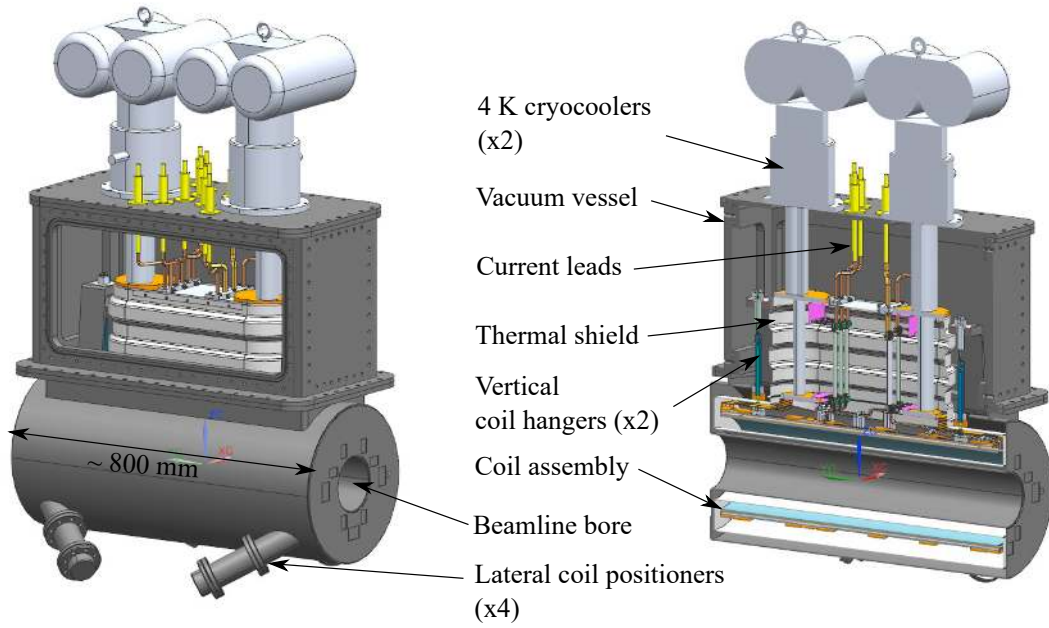
Figure 4. Model of the cryostat for the IOTA electron lens Main Solenoid.

Figure 5. Arrangement of current leads and thermal straps for conduction cooling.

where I is operating current, T_H and T_L are warm end and cold end temperatures of the resistive leads, σ is the electrical conductivity, k is the thermal conductivity, and $Q_{L,\mathrm{min}}$ is the total heat load at T_L, given by:

$$Q_{L,\mathrm{min}} = I \left(2 \int_{T_L}^{T_H} \frac{k(T)}{\sigma(T)} \, dT \right)^{1/2}. \tag{3.2}$$

Figure 6 summarizes the results of the resistive leads optimization routine. The parameters $I = 200\,\mathrm{A}$, $T_H = 300\,\mathrm{K}$, and $T_L = 50\,\mathrm{K}$ result in $Q_{L,\mathrm{min}} = 10\,\mathrm{W}$ and optimal $L/A_{\mathrm{CS}} = 2.8\,\mathrm{m^{-1}}$. The optimization used temperature dependent σ and k for phosphor bronze taken from NIST Monograph 177 [13], assuming 5% tin content by weight in the alloy. The curve in figure 6 is the temperature

profile along the length of the lead assuming 170 mm length and 61 mm^2 cross section. We note that the optimized current lead has an adiabatic boundary $Q_H = 0$ at T_H, which is a necessary condition for minimizing the total heat load at T_L through the lead [12].
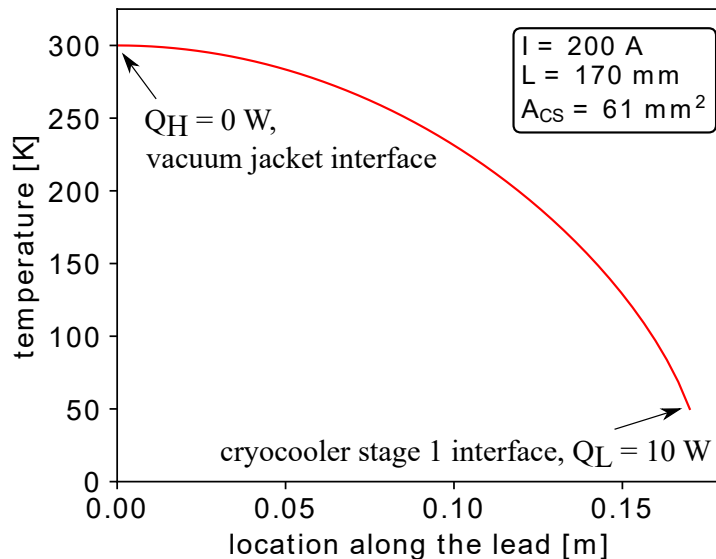
Figure 6. Results of the resistive lead design optimization.

Commercial off-the-shelf HTS-110 CryoSaver^{TM} current leads [11] are deployed between cryocooler stage 1 and stage 2. The HTS lead uses a BSSCO superconducting wire encased in a fiberglass composite body for structural integrity. The lead terminations have flat nickel plated copper endcaps with bolt holes. The selected HTS lead has current rating of 250 A at 64 K, which exceeds the design current of 200 A at the expected lead operating temperature of < 50 K.

3.3   Cryocooler conduction cooling

The conduction cooling arrangement for the current leads and the solenoid assembly is depicted in figure 5. Foil-shaped straps made of copper are used for conduction cooling. An OFHC copper strap connects stage 1 of the cryocooler to the interconnect of the resistive and HTS current leads. A sapphire washer is placed between the strap and each interconnect to electrically isolate the strap from the current leads while ensuring good thermal conductance across the contact. The washers are supplied by HTS-110 and a single washer is usable with interconnects carrying up to 1 kA. A similar OFHC copper foil strap is deployed between the cryocooler stage 2 and interconnects of the HTS-NbTi leads.

The solenoid coil assembly is connected to the cryocooler stage 2 using larger foil straps made of high purity copper (residual resistivity ratio ~500). Compared to OFHC, this copper grade possesses much higher thermal conductivity below ~ 40 K, which helps to reduce the cooldown time of the solenoid assembly to its base temperature of 4 K. Near the end of the coil assembly, the foil strap branches out into three sections that are bolted individually to the main coil, main coil support, and corrector coil support. The other termination of the strap is bolted to the cryocooler stage 2.

3.4 Thermal model

We developed a comprehensive thermal model of the Main Solenoid. The model solves the transient state heat diffusion equation to predict the solenoid's cooldown time and estimates of the heat loads expected during the operation. The material, density, and mass of cryostat components relevant to the thermal model are listed in table 4.

Table 4. Cryostat components, materials, densities and masses.

Component	Material	Density [kg/m^3]	Mass [kg]
Thermal shield	Al6061	2700	6.7
Thermal links to thermal shield	Al6061	2700	0.6
Cryocooler heat exchanger	OFHC copper	8960	2.4
Thermal shield hangers	Kevlar 49	1440	0.2
Resistive current leads	Phosphor bronze (5% Sn)	8800	0.5
Total cold mass for cryocooler stage 1			10.4
Quench protection layer	5N aluminum	2700	2.4
Superconducting cable	NbTi-Cu	8368	13.3
Epoxy	Stycast 2850	2200	1.1
Main coil support	Al6061	2700	3.5
Corrector coil support	OFHC copper	8960	10.6
Cable strain relief	Al6061	2700	1.8
Coil terminations	NbTi-Cu	8368	0.35
Magnet hangers	Kevlar 49	1440	0.2
Thermal link to coil	High purity copper (RRR500)	8960	0.6
Cryocooler heat exchanger	OFHC copper	8960	0.6
HTS lead conductor	BSSCO layer on steel substrate	8050	0.4
HTS outer insulation	G-10	1800	0.1
Total cold mass for cryocooler stage 2			34.95

The model requires temperature dependent thermal conductivities, specific heat capacities, and emissivities of the cryostat components for solving the transient heat diffusion equation. The thermal conductivities and specific heat capacities for copper, aluminum alloy, G10, Stycast 2850, and stainless steel are taken from the NIST database [14] while those for NbTi are taken from [15]. The material emissivities listed in table 5 are from ref. [16].

For bolted thermal contacts, i.e. at the two ends of the coil cooling link (see figure 5), thermal conductance is derived from the experimental data published in [17]. Figure 7a shows this data for temperatures in the range 3–300 K. Temperature dependent cooling capacity of the Cryomech PT415 cryocooler is displayed in figure 7b. The solid lines are least-squares fits to the data from ref. [18].

The thermal model uses the following assumptions:

1. Thermal shield and magnet assembly are considered as lumped masses. Spatial temperature gradients are neglected so that the cooldown time may be reasonably estimated without going into the complexity of spatial dimensions.
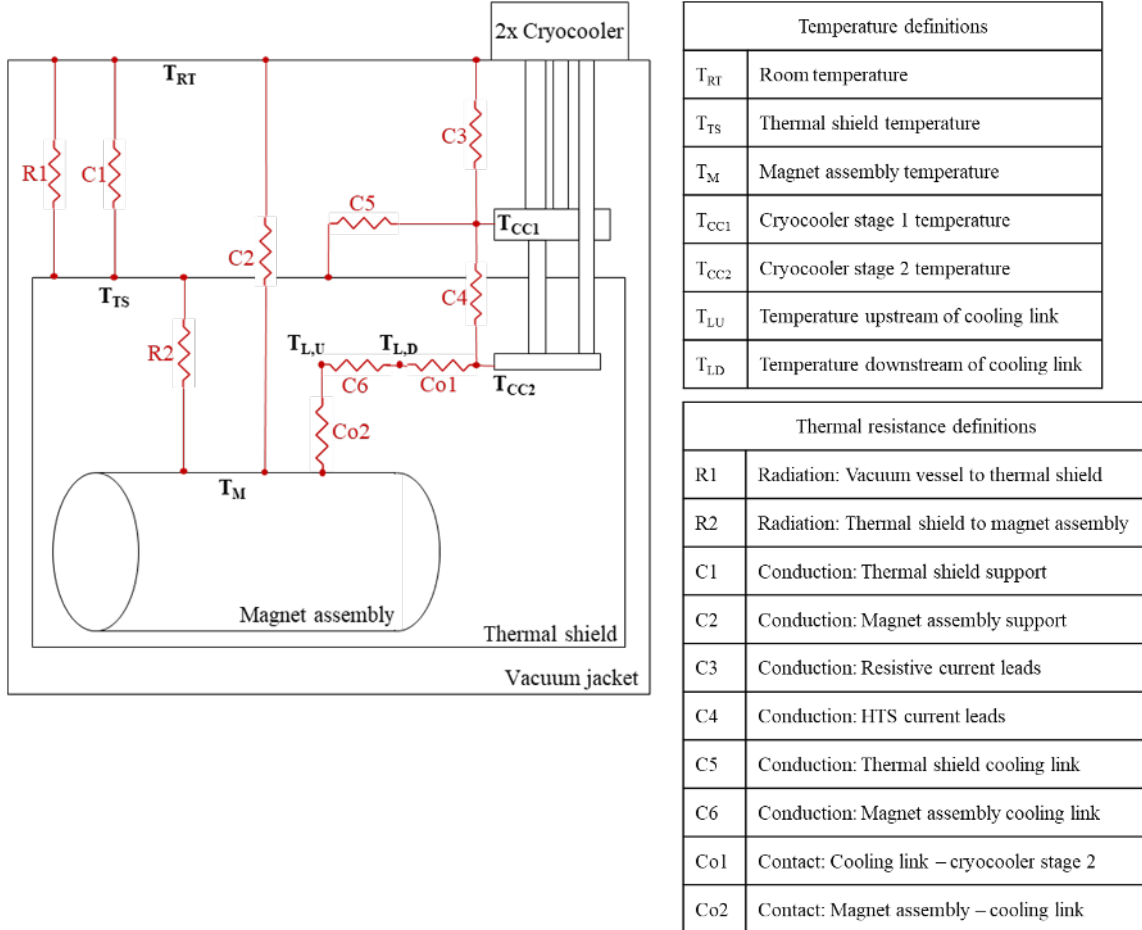
Table 5. Component surface area and emissivity relevant to the calculation of thermal radiation.

Component	Inner surface [m^2]	Outer surface [m^2]	Emissivity	Comment
Vacuum vessel	1.97	—	0.17	polished SS304
Thermal shield	1.34	1.38	0.04	polished aluminum
Solenoid assembly	0.38	0.86	0.04/0.03	inner polished aluminum / outer polished copper
Multilayer insulation (MLI)	—	—	0.03	aluminized mylar, 30 layers between vacuum vessel and thermal shield
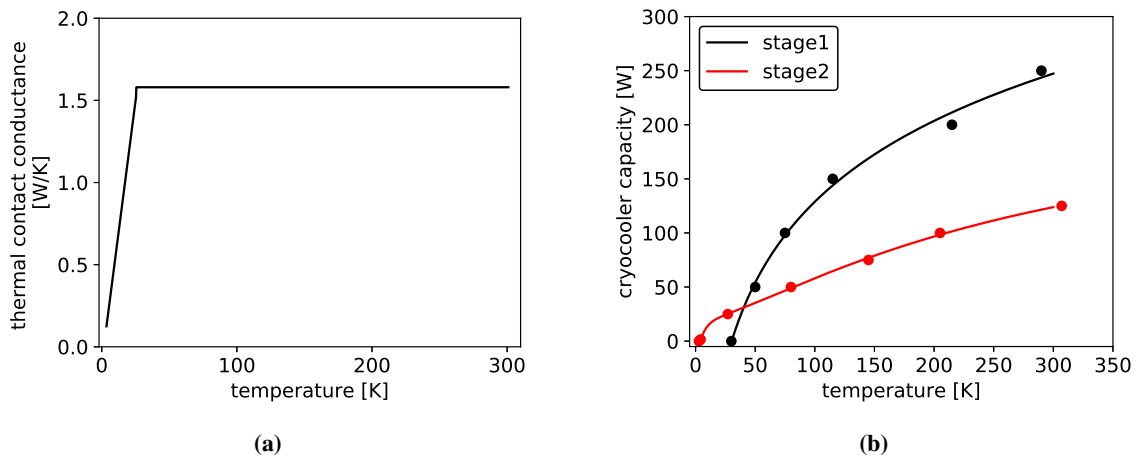
Figure 7. Temperature dependence of (a) sample thermal contact conductance of copper [17] (p. 90) and (b) Cryomech PT415 cryocooler capacity in the range 3–300 K [18].

2. Thermal masses of current leads are evaluated in the following way:
   (a) Resistive current leads at the temperature of cryocooler stage 1
   (b) HTS current leads at the temperature of cryocooler stage 2.
3. Cryocooler stages 1 and 2 cool independently — the cooling capacity of one does not depend on the temperature of the other.
4. Thermal contact conductances between the following are neglected as they are not expected to significantly influence the magnet assembly cooldown rate:
   (a) thermal shield and cryocooler stage 1
   (b) resistive current leads and cryocooler stage 1
   (c) HTS current leads and cryocooler stage 1
   (d) HTS current leads and cryocooler stage 2.
5. Thermal contact resistance is considered for the following contacts:
   (a) magnet assembly and its thermal link
   (b) the magnet assembly thermal link and cryocooler stage 2.
6. Thermal shield and magnet assembly are wrapped with 30 layers of multilayer insulation (MLI).

Figure 8 represents the principal heat transfer channels during the cooldown and operation of the solenoid. These channels, which include conduction and radiation heat transfer, are shown as a thermal resistance network. The tables in figure 8 define the temperature nodes of interest (where temperature is to be calculated) and the heat transfer channel corresponding to each thermal resistance.

Temperature definitions	
T_{RT}	Room temperature
T_{TS}	Thermal shield temperature
T_M	Magnet assembly temperature
T_{CC1}	Cryocooler stage 1 temperature
T_{CC2}	Cryocooler stage 2 temperature
T_{LU}	Temperature upstream of cooling link
T_{LD}	Temperature downstream of cooling link

Thermal resistance definitions	
R1	Radiation: Vacuum vessel to thermal shield
R2	Radiation: Thermal shield to magnet assembly
C1	Conduction: Thermal shield support
C2	Conduction: Magnet assembly support
C3	Conduction: Resistive current leads
C4	Conduction: HTS current leads
C5	Conduction: Thermal shield cooling link
C6	Conduction: Magnet assembly cooling link
Co1	Contact: Cooling link − cryocooler stage 2
Co2	Contact: Magnet assembly − cooling link

Figure 8. Schematic of the thermal model (left), definitions of temperature at locations of interest (top right), and the definitions of the thermal resistances (bottom right).

Since residual gas conduction is negligible due to high vacuum in the cryostat, the heat transfer modes are conduction through solid elements, surface to surface radiation, and heat flow across bolted contacts. The modes are mathematically defined as follows:

1. Conduction heat transfer $q_{\text{conduction}}$ between two nodes at temperatures T_1 and T_2:

$$q_{\text{conduction}}(T_1, T_2) = \frac{A_{\text{CS}}}{L} \int_{T_2}^{T_1} k(T)\, dT, \tag{3.3}$$

2. Surface-to-surface radiation $q_{\text{radiation}}$:

$$q_{\text{radiation}}(T_1, T_2) = \frac{\sigma_{SB}\left(T_1^4 - T_2^4\right)}{\frac{1-\epsilon_1}{\epsilon_1 A_1} + \frac{1}{A_2}\left(\frac{1}{\epsilon_2} + \frac{2N_{\text{MLI}}}{\epsilon_{\text{MLI}}} - N_{\text{MLI}}\right)}, \tag{3.4}$$

where σ_{SB} is the Stefan-Boltzmann constant, A_i and ϵ_i are the surface area and the emissivity of surface i, and N_{MLI} is the number of MLI blankets between the two surfaces.

3. The rate of heat transfer across a bolted contact, $q_{contact}$, with thermal conductance $C_{contact}$:

$$q_{contact}(T_1, T_2) = \int_{T_2}^{T_1} C_{contact}(T)\, dT. \tag{3.5}$$

An energy balance applied to each of the six temperature nodes defined in figure 8 leads to the system of equations:

$$\left(\sum mc_p(T_i)\right)\frac{dT_i}{dt} = \left(\sum q_{in}\right)_i - \left(\sum q_{out}\right)_i \qquad i = [\text{TS}, \text{CC2}, \text{M}, \text{LU}, \text{LD}, \text{CC1}], \tag{3.6}$$

where the left-hand side represents the rate of change of internal energy at each node and the right-hand side denotes the net rate of heat flow through the node (total heat in minus total heat out). The system of equations (3.6) is a coupled system of six ordinary differential equations, where the heat transfer rates are strongly dependent on the unknown temperatures. The system is solved using the `odeint` library available with scientific `Python`.

The thermal model results are summarized in figure 9 and tables 6 and 7. With the existing configuration, the solenoid assembly takes 21 h to cool down from room temperature to 4 K. The cooldown rate is primarily governed by the total thermal conductance of the coil cooling link, which comprises two thermal contacts (link-coil and link-cryocooler) and bulk conductance of the cooling link. Figure 9a shows that the temperature drop across the link ($T_{LD} - T_{LU}$) is much greater than that across the contacts ($T_M - T_{LD}$ and $T_{LU} - T_{CC2}$), indicating that the bulk imposes the most thermal resistance in the cooling link. The bulk thermal resistance can be reduced by increasing the cross section of the coil cooling link. For instance, figure 9b shows the cooldown curves that would results from a link with twice the cross section. The solenoid assembly in this case cools down in 18 h. For even faster cooldown, the cooling link thermal resistance can be further reduced by increasing its cross section or by reducing the contact resistance by applying thermal interface materials (for example, indium foil) at the cooling link bolted contacts. In any case, cooldown times below 24 h are considered acceptable.

Table 6 and table 7 list the steady-state temperatures and heat loads on the Main Solenoid assembly. Two cases are considered: when the magnet is not powered, $I = 0$ A, and when the magnet is fully powered, $I = 200$ A. In both the cases, the temperatures are < 4.5 K, which is suitable for solenoid operation. Furthermore, the heat loads are well within the cooling budget of the PT415 cryocoolers.

4 Quench analysis

A quench can result from a part of the superconducting coil warming above NbTi superconducting transition temperature. Following a quench, NbTi will turn resistive and a large portion of the circulating current will transfer to the copper stabilizer in the conductor. The current (and stored energy) will then dissipate in the coil resistance causing the coil (a) to further warm up and (b) to induce internal voltage. Determining the peak coil temperature and peak coil voltage following a quench are two goals of the present quench analysis. We note that the low operating current of 200 A
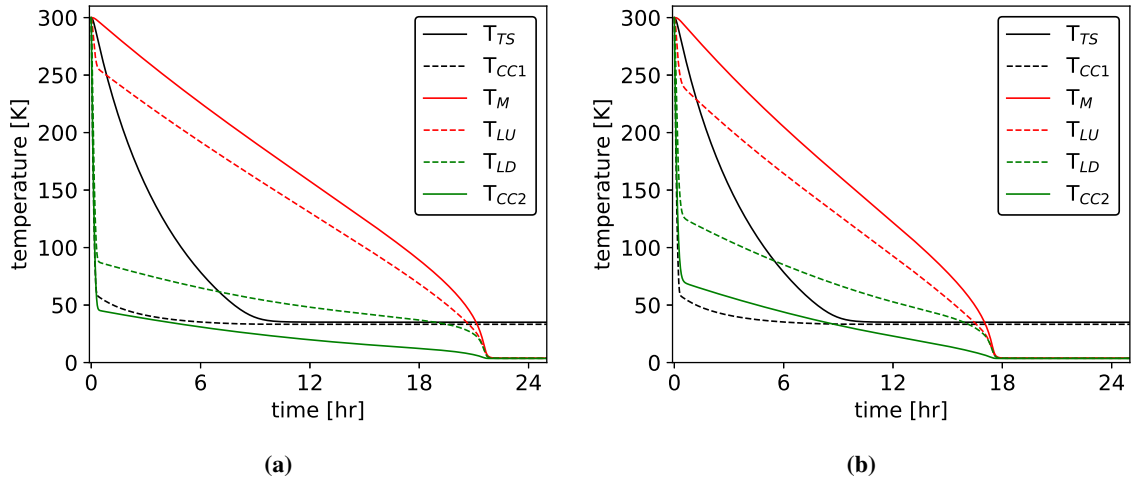
Figure 9. Solenoid cooldown profile with (a) existing coil cooling link and (b) a link with twice the cross section.

Table 6. Main Solenoid steady state temperature, assuming room temperature RT = 300 K.

Location	Steady-state temperature [K]	
	$I = 0\,\text{A}$	$I = 200\,\text{A}$
T_{CC1}	33.3	48.1
T_{TS}	35.1	49.5
T_{CC2}	3.56	3.62
T_{LD}	3.71	3.76
T_{LU}	3.72	3.77
T_{M}	3.86	3.9

Table 7. Main Solenoid steady state heat load, assuming room temperature RT = 300 K.

Heat transfer channel	Steady-state heat load [W]	
	$I = 0\,\text{A}$	$I = 200\,\text{A}$
Hanger conduction, RT to TS	0.04	0.04
Radiation, RT to TS	0.32	0.32
Resistive lead conduction + Joule dissipation, RT to CC1	20.1	100
Total to CC1	20.5	100.4
Hanger conduction, RT to Magnet	0.02	0.02
Radiation, TS to Magnet	3.7×10^{-5}	1.5×10^{-4}
HTS lead conduction, CC1 to CC2	0.16	0.34
Total to CC2	0.18	0.36

compared to the critical current of 550 A for the Luvata cable can provide margin of safety for the coil. A quench analysis is carried out to not only ascertain this but also to understand requirements for an adequate quench detection and protection system.
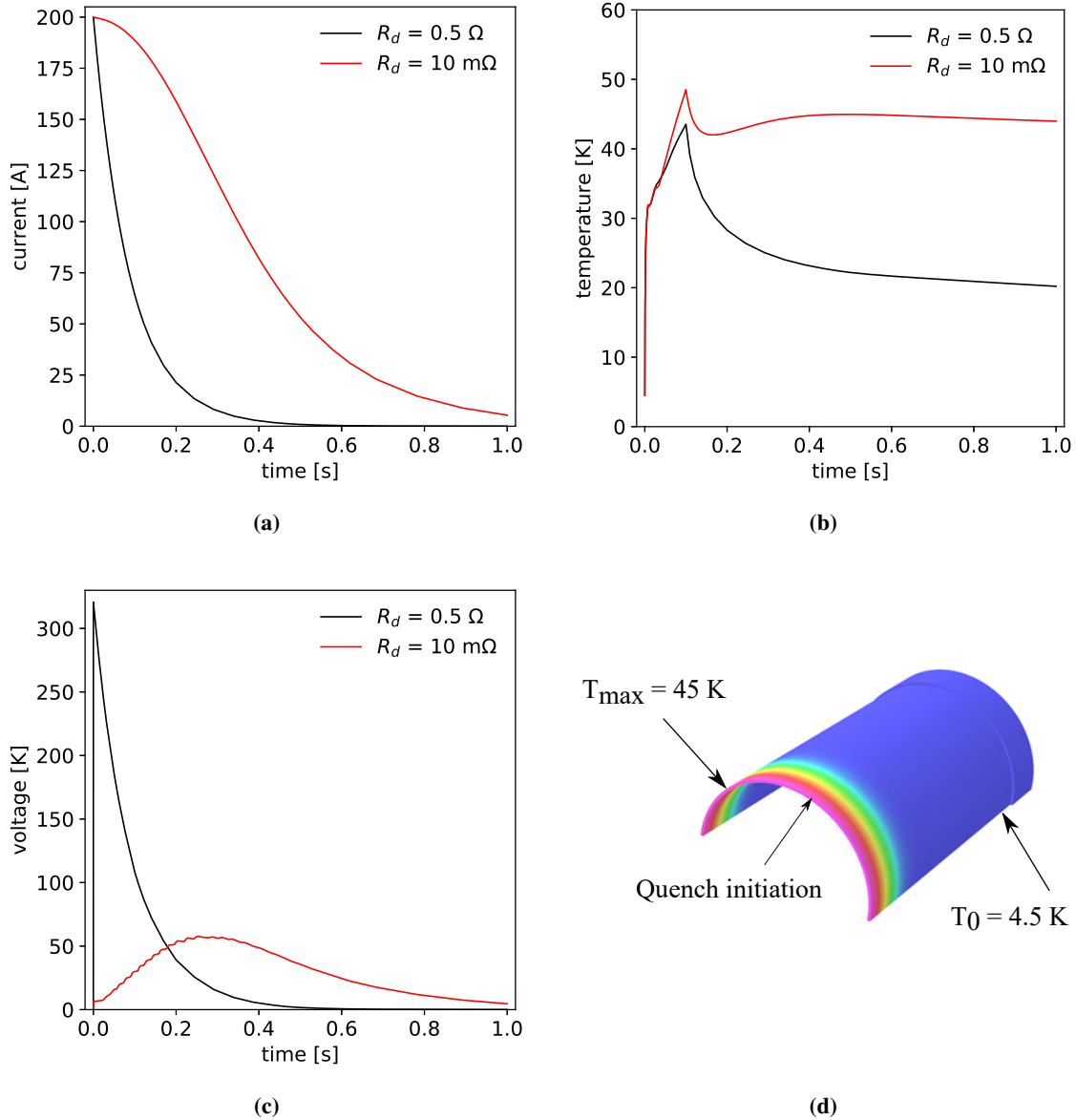
Figure 10. Quench simulation results depicting (a) current decay, (b) coil temperature rise, (c) coil voltage rise and (d) coil temperature profile 2 s after the quench with a 10 mΩ dump resistor.

Quench parameters are calculated using OPERA 3D QUENCH code following the conservative adiabatic coil heating approach [9, 19, 20]. This approach assumes that immediately after a quench the current supply turns off and an external dump resistor comes in series with the coil. These processes can be activated by a quench protection system. The circulating current (and stored energy) then dissipates in the coil and the dump resistor. The present simulations use two values of the dump resistor, 0.5 Ω and 10 mΩ along with temperature dependent thermal conductivity and

heat capacity of the conductor. The quench is initiated in the middle of the solenoid by a short heater pulse that locally warms the coil.

Figure 10 presents the time profiles of coil current, temperature, and voltage following the simulated quench. The transients in all the three parameters decay within one second of the quench initiation. With the smaller dump resistor the current decay takes longer and the coil gets to warmer temperature. However, the coil peak voltage is smaller. The choice of the dump resistor thus involves a trade-off between the peak coil temperature and peak coil voltage. Nonetheless, both upper values of peak coil voltage (320 V) and peak coil temperature (42 K) are reasonable for epoxy impregnated coils such as the one being designed for the Main Solenoid. Figure 10d depicts the 3D temperature profile in the coil with a 10 mΩ dump resistor, 2 s after quench. This is well beyond the timescale of the transients and so can be considered as a steady state. The temperature profile in the coil shows that only a small part of the coil actually warms up to 45 K, while a large section still is at the base temperature of 4.5 K. This indicates that after recovery from the quench the coil can be cooled back to its base temperature within a reasonably short time with cryocooler conduction cooling.

The present quench analysis neglects the effects of eddy currents induced in the aluminum quench protection layer of the coil assembly (see figure 2). These eddy currents are expected to further lower the peak quench parameters in the coil [21].

5   Summary and outlook

We presented the first results of the design of a superconducting solenoid for the IOTA electron lens at Fermilab. The design is based on commercially available NbTi cable and on 4 K pulse tube cryocoolers for conduction cooling. The solenoid assembly is compact, lightweight, and more energy efficient compared to a resistive solenoid. A detailed thermal model shows that the static and dynamic heat loads in the solenoid are well within the cooling capacity of the selected cryocoolers. The thermal model further predicts that the solenoid assembly would cool down to its operating temperature in less than a day. The quench analysis using an external dump resistor shows that the coil would be thermally stable during a quench event and be able to cool back down in a few hours after recovering from the quench.

Future work includes refining the electromagnetic design to satisfy the field quality requirements and a detailed engineering design, followed by manufacture, testing, and commissioning in the IOTA storage ring.

References

[1] S. Antipov et al., *IOTA (Integrable Optics Test Accelerator): Facility and Experimental Beam Physics Program*, 2017 *JINST* **12** T03002 [arXiv:1612.06289].

[2] G. Stancari, *Applications of electron lenses: scraping of high-power beams, beam-beam compensation, and nonlinear optics*, *AIP Conf. Proc.* **1777** (2016) 100007 [arXiv:1409.3615].

[3] G. Stancari et al., *Beam physics research with the IOTA electron lens: Status and plans*, in *ICFA Beam Dynamics Newsletter#81* (2021).

[4] V. Shiltsev et al., *Tevatron Electron Lenses: Design and Operation*, *Phys. Rev. ST Accel. Beams* **11** (2008) 103501 [arXiv:0808.1542].

[5] M. Anerella, J. Tuozzolo, P. Wanderer, W. Fischer, R. Gupta, A. Jain et al., *Mechanical design and construction of superconducting e-lens solenoid magnet system for RHIC head-on beam-beam compensation*, *IEEE Trans. Appl. Supercond.* **24** (2014) 1.

[6] D. Mirarchi, H. Garcia Morales, A. Mereghetti, S. Redaelli, J. Wagner, W. Fischer et al., *Hollow electron-lens assisted collimation and plans for the LHC*, in proceedings of the *61st ICFA Advanced Beam Dynamics Workshop on High-Intensity and High-Brightness Hadron Beams*, Daejeon, Korea, 17–22 June 2018, pp. 92–98.

[7] A. Kalimov, C. Muehle, D. Ondreka, K. Schulte-Urlichs and P. Spiller, *Optimization of a solenoid for an electron lens in SIS18*, *IEEE Trans. Appl. Supercond.* **30** (2020) 1.

[8] A. Dudarev, M. Doser, D. Perini and H. ten Kate, *Design of a superconducting magnet system for the AEGIS experiment at CERN*, *IEEE Trans. Appl. Supercond.* **21** (2011) 1721.

[9] M.N. Wilson, *Superconducting Magnets*, Clarendon Press, Oxford (1983).

[10] R.F. Barron, *Cryogenic Systems*, Oxford University Press, Oxford (1985).

[11] *HTS-110 Cryosaver^{TM} current leads*, https://www.scottautomation.com/hts-110/products/cryosaver-current-leads.

[12] R. McFee, *Optimum input leads for cryogenic apparatus*, *Rev. Sci. Instrum.* **30** (1959) 98.

[13] N.J. Simon, E.S. Drexler and R.P. Reed, *Properties of copper and copper alloys at cryogenic temperature*, Monograph 177, NIST (1992).

[14] *NIST cryogenic material properties database*, https://trc.nist.gov/cryogenics/materials/materialproperties.htm.

[15] A. Davies, *Material properties data for heat transfer modeling in Nb$_3$Sn magnets*, 2011.

[16] F.P. Incropera and D.P. DeWitt, *Fundamentals of Heat and Mass Transfer*, John Wiley and Sons, Inc. (1996).

[17] M.J. Nilles, *Thermal and Electrical Contact Resistance of OFHC Cu from 4 K to 290 K*, Ph.D. thesis, University of Wisconsin Madison (1986).

[18] M.A. Green, S.S. Chouhan, C. Wang and A.F. Zeller, *Second stage cooling from a Cryomech PT415 cooler at second stage temperatures up to 300 K with cooling on the first-stage from 0 to 250 W*, *IOP Conf. Ser. Mater. Sci. Eng.* **101** (2015) 012002.

[19] D.B. Montgomery, *Solenoid Magnet Design*, John Wiley and Sons, Inc. (1969).

[20] Y. Iwasa, *Case Studies in Superconducting Magnets*, Plenum Press (1994).

[21] V. Kashikhin, A. Bross, R. Carcagno, D. Orris and D. Turrioni, *MuCool superconducting solenoid quench simulations and test stand at FNAL*, *IEEE Trans. Appl. Supercond.* **23** (2013) 4101704.